Spintronics Meets Density Matrix Renormalization Group: Quantum Spin-Torque-Driven Nonclassical Magnetization Reversal and Dynamical Buildup of Long-Range Entanglement

Marko D. Petrović[⬤],[1] Priyanka Mondal,[1] Adrian E. Feiguin[⬤],[2] Petr Plecháč[⬤],[3] and Branislav K. Nikolić[⬤][1,*]

[1]*Department of Physics and Astronomy, University of Delaware, Newark, Delaware 19716, USA*
[2]*Department of Physics, Northeastern University, Boston, Massachusetts 02115, USA*
[3]*Department of Mathematical Sciences, University of Delaware, Newark, Delaware 19716, USA*

We introduce the time-dependent density matrix renormalization group (tDMRG) as a solution to a *long-standing* problem in spintronics—how to describe spin-transfer torque (STT) between flowing spins of conduction electrons and localized spins within a magnetic material by treating the dynamics of both spin species *fully* quantum mechanically. In contrast to conventional Slonczewski-Berger STT, where the localized spins are viewed as classical vectors obeying the Landau-Lifshitz-Gilbert equation and where their STT-driven dynamics is initiated *only* when the spin polarization of flowing electrons and localized spins are *noncollinear*, quantum STT can occur when these vectors are *collinear but antiparallel*. Using tDMRG, we simulate the time evolution of a many-body quantum state of electrons and localized spins, where the former are injected as a spin-polarized current pulse while the latter comprise a quantum Heisenberg ferromagnetic metallic (FM) spin-$\frac{1}{2}$ *XXZ* chain initially in the ground state with spin polarization antiparallel to that of injected electrons. The quantum STT reverses the direction of localized spins, but without rotation from the initial orientation, when the number of injected electrons exceeds the number of localized spins. Such *nonclassical reversal*, which is absent from Landau-Lifshitz-Gilbert dynamics, is strikingly inhomogeneous across the FM chain, and it can be accompanied by reduction of the magnetization associated with localized spins, even to zero at specific locations. This feature arises because quantum STT generates a highly entangled nonequilibrium many-body state of all flowing and localized spins, despite starting from the initially unentangled ground state of a mundane FM. Furthermore, the mutual information between localized spins at the FM edges remains nonzero even at infinite separation as the signature of dynamical buildup of *long-range* entanglement. The growth in time of entanglement entropy differentiates between the quantum and conventional (i.e., noncollinear) setups for STT, reaching a much larger asymptotic value in the former case.

I. INTRODUCTION

The conventional spin-transfer torque (STT) has been at the forefront of basic [1] and applied [2] research in spintronics since the seminal theoretical predictions of Slonczewski [3] and Berger [4] and its experimental confirmations, initially in spin valves [5–7] and later in magnetic tunnel junctions [8–10]. Its *key requirement* is that the spin polarization of flowing conduction electrons injected into a ferromagnetic metal (FM) must be *noncollinear* to FM magnetization, as illustrated in Fig. 1(b).

*[*]bnikolic@udel.edu

Thus, it came as a great surprise when current-driven magnetization dynamics was recently observed at ultralow $T \sim 1$ K temperatures [11,12] in FM-polarizer/normal-metal/FM-analyzer spin valves with *collinear* magnetizations. Although thermal fluctuations of magnetization can create the required noncollinearity of magnetizations of two ferromagnetic layers within spin valves (or magnetic tunnel junctions) at room temperature [12], they are frozen at ultralow temperatures of the experiment in Ref. [11]. Thus, the effect observed in Ref. [11] is dubbed "quantum STT" [12] and believed to be dissociated from conventional STT. In fact, few earlier experiments [13–15] have reported current-driven excitation of high-energy magnons (with ~ 1 THz frequencies, which is orders of magnitude higher than typical ~ 1 GHz magnetization dynamics driven by conventional STT), suggesting that collinear [but antiparallel, as illustrated in Fig. 1(c)] spin polarization of flowing conduction electrons and localized
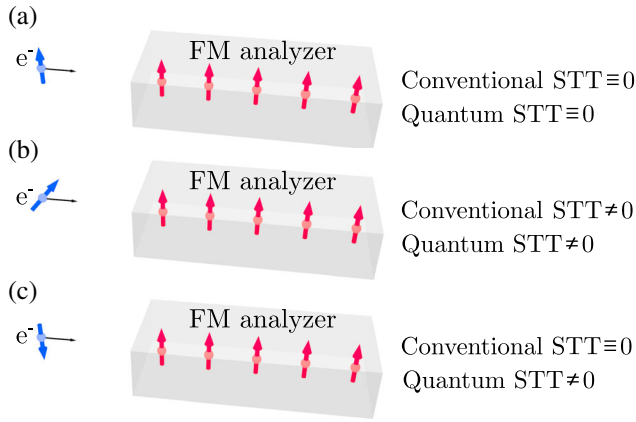
FIG. 1. Illustration of three types of geometries of flowing conduction electron spins (blue arrow), assumed to be polarized by the FM-polarizer layer (not shown explicitly), with respect to localized spins (red arrows) within the FM-analyzer layer onto which electrons are impinging: (a) parallel; (b) noncollinear; and (c) antiparallel. The conventional STT [1,3,4] is nonzero only in (b), while quantum STT is nonzero in both (b) and (c). Blue and red arrows represent expectation values of the corresponding quantum-mechanical spin operators. For conventional STT, red arrows are modeled as classical vectors of fixed length [1,16,17], whose time evolution due to conventional STT is animated by three TDNEGF + LLG-computed movies in Supplemental Material [18] [showing no dynamics for (a) and (c)].

magnetic moments drives the dynamics of the latter, which is, therefore, also apparently dissociated from conventional STT.

The "standard model" [1] of conventional STT involves localized magnetic moments $\mathbf{M}_i$, viewed as *classical vectors of fixed length*, which interact with a nonequilibrium electronic spin density $\mathbf{s}_i$, computed by some steady-state [19–22] or time-dependent [16,23,24] single-particle quantum transport formalism. The nonequilibrium electronic spin density is then fed into the Landau-Lifshitz-Gilbert (LLG) equation [17] for $\mathbf{M}_i(t)$ in order to include Slonczewski-Berger STT $\propto \mathbf{s}_i \times \mathbf{M}_i$. Thus, in the context of collinear spin valve setup of Ref. [11], where the conventional Slonczewski-Berger STT $\propto \mathbf{s}_i \times \mathbf{M}_i \equiv 0$, the standard model predicts *no effect*. This result is also illustrated by static $\mathbf{M}_i(t)$, despite injected current pulse, in the movies in Supplemental Material [18] animating Figs. 1(a) and 1(c), which are obtained from time-dependent nonequilibrium Green function combined with LLG (TDNEGF + LLG) simulations [16,23,24] as an example of *quantum*-for-electrons–*classical*-for-localized-spins approach falling into the category of the standard model. In contrast, $\mathbf{M}_i(t)$ exhibit nontrivial dynamics in the TDNEGF + LLG-computed movie [18] which animates Fig. 1(b), as expected from conventional STT $\propto \mathbf{s}_i \times \mathbf{M}_i \neq 0$ being nonzero in the noncollinear setup in Fig. 1(b).

Let us recall that, in general, the LLG description [17] of the dynamics of localized spins is justified [25,26] only in the limit of large localized spins $S \to \infty$ and $\hbar \to 0$ (while

$S \times \hbar \to 1$), as well as in the *absence of entanglement* in many-body quantum state of localized spins. Entanglement describes genuinely quantum and nonlocal correlations between different parts of a physical system. While the LLG description often captures experiments on realistic materials where S is finite, it inevitably becomes inapplicable [25,26] in the presence of such many-body entanglement [27,28], because the length $|\mathbf{M}_i(t)|$ is then changing in time with smaller values signifying higher entanglement. For example, even if we start with a separable (unentangled) state of N_{FM} localized spins as the ground state of the FM-analyzer at $t = 0$, $|\Phi(t = 0)\rangle_{\text{lspins}} = |\downarrow_1 \downarrow_2 \ldots \downarrow_{N_{FM}}\rangle$, spin-polarized current injection in the collinear setup in Fig. 1(c) or noncollinear setup in Fig. 1(b) eventually generates superpositions [Eq. (15)] of such separable states. This result means that the quantum state of localized spins will become both mixed [29], due to being a subsystem of a larger composite quantum system which includes flowing electrons, and entangled with its measures of entanglement monotonically increasing in time (Fig. 7). In general, nonequilibrium quantum systems left unobserved (i.e., without their unitary evolution being punctuated by nonunitary projective measurements) tend to evolve toward states of higher entanglement [30], as observed experimentally [31] at sufficiently low temperature ensuring that decoherence due to external environment is suppressed. In addition, $|\Phi(t = 0)\rangle_{\text{lspins}}$ could be entangled from the outset, as is the case of strongly electron-correlated and/or exotic solid-state materials such as quantum antiferromagnets [32,33], Mott insulators [32], and quantum spin liquids [34]—in all three cases, many-body entanglement [27,28] in the ground state in equilibrium leads to $\mathbf{M}_i(t = 0) \equiv 0$ so that one again encounters a situation where the conventional Slonczewski-Berger STT $\propto \mathbf{s}_i \times \mathbf{M}_i \equiv 0$ cannot be initiated. Thus, either due to entanglement already present in $|\Phi(t = 0)\rangle_{\text{lspins}}$ or due to dynamical buildup of entanglement in the time-dependent quantum state, the LLG equation for localized spins—which evolves them as classical vectors while assuming that their trajectories mimic trajectories of the quantum-mechanical spin expectation values—becomes inapplicable. Instead, time evolution of localized spins *must* be treated quantum mechanically with their individual expectation values $\mathbf{S}_i(t)$ [or $\mathbf{M}_i(t) \propto \mathbf{S}_i(t)$] *calculated only at the end*—we term any such situation where the current-driven dynamics of localized spins must be described fully quantum mechanically as *quantum STT*.

Surprisingly, despite a long history of STT, an established fully quantum-mechanical framework for coupled dynamics of localized spins and flowing electron spins, as well as transfer of spin angular momentum between them, is still lacking [11,12,35,36]. Since both electrons and localized spins have to be evolved quantum mechanically by such a framework, it invariably has to be constructed
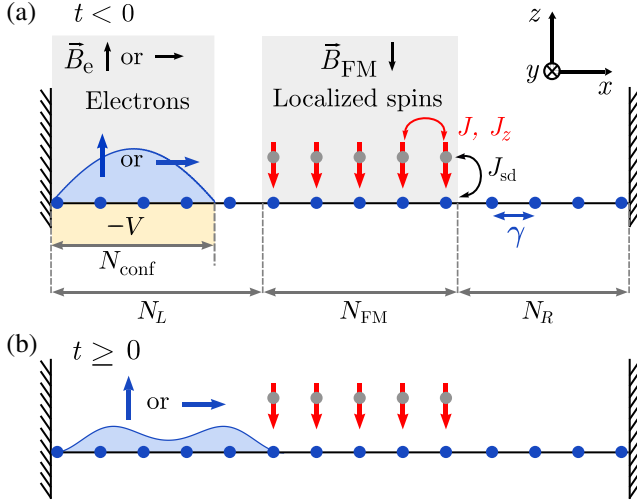
FIG. 2. Schematic view of a two-terminal setup for tDMRG calculations where a 1D tight-binding chain (blue dots) of $N = 75$ sites, with electron nearest-neighbor hopping γ between all sites, hosts $N_{\mathrm{FM}} = 5$ localized spins-$\frac{1}{2}$ (red arrows) comprising a ferromagnetic quantum Heisenberg XXZ chain. The initial $N_L = 35$ sites within the left fermionic lead also include $N_{\mathrm{conf}} = 10$ sites where the confining potential V is applied to $N_e \in \{1, 5, 8\}$ electrons filling those sites. For $t < 0$, external magnetic fields $\mathbf{B}_e$ and $\mathbf{B}_{\mathrm{FM}}$ polarize electron spins along the $+z$ axis or $+x$ axis and localized spins along the $-z$ axis, respectively. For $t \geq 0$, both magnetic fields and the confining potential are switched off, so that electrons spread from left to right, as also animated by the tDMRG-computed movie in Supplemental Material [18].

using the tools of nonequilibrium quantum many-body theory. A handful of recent theoretical studies [33,37–40] offer insights into possible microscopic mechanisms of quantum STT. However, they rely on either (i) a mapping of original operators of localized spins to bosonic operators and additional approximations [41,42] that *do not* [43] allow one to track the time evolution of localized spins once they deviate too far from the initial orientation set by the anisotropy axis [37,38] or (ii) considering *only one* injected spin-polarized electron [33,39,40], which is insufficient to reverse many localized spins because of demand posed by spin angular momentum conservation.

In this study, we introduce the adaptive time-dependent density matrix renormalization group (tDMRG) [44–48] as a numerical framework capable of describing quantum and conventional STT on the same footing. Since this simulation method works directly with the original quantum-mechanical operators of the localized spins, it can capture reversal of localized spins due to STT which is highly sought in spintronic applications [1,2,22,24]. We demonstrate this reversal by applying the tDMRG framework to a one-dimensional (1D) setup depicted in Fig. 2, where a quantum Heisenberg FM spin-$\frac{1}{2}$ XXZ chain is attached to the left (L) and right (R) fermionic leads [49,50] modeled as 1D tight-binding chains of finite length. The *nonzero* electron hopping between the sites of the XXZ chain means
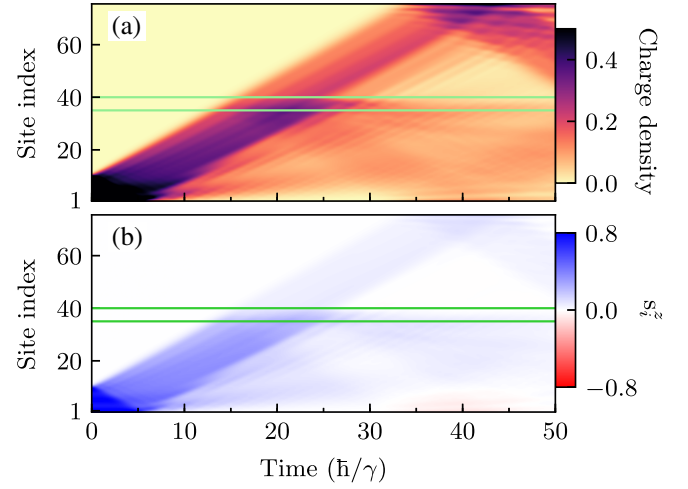

FIG. 3. Spatiotemporal profiles of electronic (a) charge density and (b) spin-z density for a spin-polarized current pulse composed of $N_e = 8$ electrons injected into the FM region in Fig. 2. The green horizontal lines in both panels mark the first and the last localized spin of the FM region. Electrons are initially ($t < 0$) spin polarized along the $+z$ axis, while localized spins are polarized along the $-z$ axis. The strength of sd exchange interaction between electron spin and localized spins is $J_{\mathrm{sd}} = 0.5\gamma$. Both panels are animated as the tDMRG-computed movie in Supplemental Material [18] for $J_{\mathrm{sd}} = 0.5\gamma$ and $J_{\mathrm{sd}} = 2.0\gamma$.

that the FM chain models the *metallic* FM-analyzer layer that is receiving STT. From the viewpoint of the physics of strongly correlated electrons, this model can also be interpreted as a Kondo-Heisenberg chain [51] sandwiched by fermionic leads, with ferromagnetic exchange interaction between localized spins, as well as between localized spins and injected flowing electrons.

The role of the FM-polarizer layer is simulated by filling $N_{\mathrm{conf}} = 10$ sites within the L lead with $N_e \in \{1, 5, 8\}$ electrons, which are spin polarized in a desired direction by applying an external magnetic field $\mathbf{B}_e$ [see Fig. 2(a) depicting the region where this field is applied] in that direction. They are also confined into a quantum well for times $t < 0$, as illustrated in Fig. 2(a). By removing the confining potential for times $t \geq 0$, electrons spread into the region of the localized FM moments, as illustrated in Fig. 2(b), simulated in Fig. 3, and animated in the tDMRG-computed movie in Supplemental Material [18]. This protocol mimics injection of a spin-polarized current pulse often employed in STT-operated spintronic devices [1,2,22,24]. Prior to explaining our principal results in Figs. 3–8 for the STT-driven quantum dynamics of the local magnetization across the FM chain, we first introduce useful concepts and necessary notation.

II. MODEL HAMILTONIAN

The setup illustrated in Fig. 2 is a 1D chain of N sites where electrons and localized spins are described by the Hamiltonian

$$\hat{H} = \hat{H}_e + \hat{H}_{\text{lspins}} + \hat{H}_{e-\text{lspins}} + \hat{H}_{V,\mathbf{B}}(t < 0). \quad (1)$$

The tight-binding Hamiltonian for electrons

$$\hat{H}_e = -\gamma \sum_{i=1}^{N-1} (\hat{c}_{i\uparrow}^{\dagger} \hat{c}_{i+1\uparrow} + \hat{c}_{i\downarrow}^{\dagger} \hat{c}_{i+1\downarrow} + \text{H.c.}) \quad (2)$$

operates on all $N = 75$ sites, where $\hat{c}_{i\sigma}^{\dagger}$ ($\hat{c}_{i\sigma}$) creates (annihilates) an electron with spin $\sigma = \uparrow, \downarrow$ on site i. The nearest-neighbor (NN) hopping parameter $\gamma = 1$ eV sets a unit of energy. Each site hosts one of the four possible electronic quantum states—empty $|0\rangle$, spin-up $|\uparrow\rangle = \hat{c}_{i\uparrow}^{\dagger}|0\rangle$, spin-down $|\downarrow\rangle = \hat{c}_{i\downarrow}^{\dagger}|0\rangle$, and doubly occupied $|\uparrow\downarrow\rangle = \hat{c}_{i\uparrow}^{\dagger}\hat{c}_{i\downarrow}^{\dagger}|0\rangle$—from which one can construct 4^N many-body states that span the Fock space $\mathcal{F}_e$. The operators for the total number of electrons, $\hat{N}_e = \sum_{i=1}^{N} \hat{n}_i$, and total electron spin along the α axis, $\hat{s}_e^{\alpha} = \sum_{i=1}^{N} \hat{s}_i^{\alpha}$, are given by the sums of local (per-site) charge and spin density operators, $\hat{n}_i = \sum_{\sigma=\{\uparrow,\downarrow\}} \hat{c}_{i\sigma}^{\dagger}\hat{c}_{i\sigma}$ and $\hat{s}_i^{\alpha} = \sum_{\sigma=\{\uparrow,\downarrow\}} \hat{c}_{i\sigma}^{\dagger}\hat{\sigma}_{\sigma\sigma'}^{\alpha}\hat{c}_{i\sigma'}$, respectively, where $\hat{\sigma}^{\alpha}$ is the Pauli matrix. Out of $N = N_L + N_{\text{FM}} + N_R$ sites in Fig. 2, the first $N_L = 35$ belong to the L fermionic lead, and the last $N_R = 35$ belong to the R fermionic lead.

The middle $N_{\text{FM}} = 5$ sites host localized spins whose mutual interaction is described by ferromagnetic *XXZ* spin-$\frac{1}{2}$ quantum Heisenberg Hamiltonian

$$\hat{H}_{\text{lspins}} = -\sum_{i=1}^{N_{\text{FM}}-1} [J_z \hat{S}_i^z \cdot \hat{S}_{i+1}^z + J(\hat{S}_i^x \cdot \hat{S}_{i+1}^x + \hat{S}_i^y \cdot \hat{S}_{i+1}^y)].$$

$$(3)$$

Here, $\hat{S}_i^{\alpha} = \hat{I}_1 \otimes \cdots \otimes \hat{\sigma}^{\alpha} \otimes \cdots \otimes \hat{I}_{N_{\text{FM}}}$ acts nontrivially only on the Hilbert space $\mathcal{H}_i$ of localized spin at site i; $\hat{I}_j$ is the unit operator in $\mathcal{H}_j$; and the NN exchange interactions between localized spins are $J = 0.1\gamma$ and $J_z = 0.1005\gamma$, thereby including anisotropy along the z axis. The $2^{N_{\text{FM}}}$-dimensional Hilbert space of all localized spins is constructed as $\mathcal{H}_{\text{lspins}} = \mathcal{H}_1 \otimes \mathcal{H}_2 \otimes \cdots \otimes \mathcal{H}_{N_{\text{FM}}}$. Thus, the total Hamiltonian in Eq. (1) acts on the space $\mathcal{F}_e \otimes \mathcal{H}_{\text{lspins}}$, where the interaction between conduction electron spins and localized spins is described by

$$\hat{H}_{e-\text{lspins}} = -\sum_{i=1}^{N_{\text{FM}}} J_{\text{sd}}(\hat{s}_{i+N_L}^x \cdot \hat{S}_i^x + \hat{s}_{i+N_L}^y \cdot \hat{S}_i^y + \hat{s}_{i+N_L}^z \cdot \hat{S}_i^z).$$

$$(4)$$

Here, $J_{\text{sd}} = 0.5\gamma$ (the tDMRG-computed movie in Supplemental Material [18] shows an additional case with $J_{\text{sd}} = 2.0\gamma$) is interpreted as either *sd* [1] or Kondo

ferromagnetic exchange [51] interaction in the fields of spintronics or strongly correlated electrons, respectively.

For the purpose of preparing a many-electron spin-polarized current pulse, we employ the following term:

$$\hat{H}_{V,\mathbf{B}}(t < 0) = -V \sum_{i=1}^{N_{\text{conf}}} (\hat{c}_{i\uparrow}^{\dagger}\hat{c}_{i\uparrow} + \hat{c}_{i\downarrow}^{\dagger}\hat{c}_{i\downarrow})$$

$$-\sum_{i=1}^{N_{\text{conf}}} g\mu_B \hat{\mathbf{s}}_i \cdot \mathbf{B}_e - \sum_{i=1}^{N_{\text{FM}}} g\mu_B \hat{\mathbf{S}}_i \cdot \mathbf{B}_{\text{FM}} \quad (5)$$

in Eq. (1) which acts at times $t < 0$ and is used only once to initialize the system. The first term in Eq. (5) is a confining on-site potential of magnitude $V = 10\gamma$ acting within the first $N_{\text{conf}} = 10$ sites of $N_L = 35$ sites of the L fermionic lead, as illustrated in Fig. 2(a). In addition, the second term in Eq. (5) polarizes spins of the confined electrons, via an external magnetic field $|g\mu_B\mathbf{B}_e| = 100\gamma$, along the $+z$ axis for the collinear setup of quantum STT analyzed in Figs. 3, 4, 6(a), 6(b), 7, and 8, as well as in the tDMRG-computed movie in Supplemental Material [18]; or it polarizes spins of the confined electrons along the $+x$ axis for the noncollinear setup of conventional STT [1] analyzed in Figs. 5, 6(c)–6(e), and 7. The third term in Eq. (5) is employed to polarize the localized spins along the $-z$ axis using an external magnetic field $|g\mu_B\mathbf{B}_{\text{FM}}| = 100\gamma$. The electron gyromagnetic ratio is denoted by g, and μ_B is the Bohr magneton.

III. TDMRG METHODOLOGY ADAPTED TO QUANTUM SPIN-TRANSFER TORQUE

The exact time evolution of the system in Fig. 2 can, in principle, be obtained by brute-force application of the evolution operator for sufficiently small time step δt

$$|\Psi(t + \delta t)\rangle = e^{-i\hat{H}\delta t/\hbar}|\Psi(t)\rangle. \quad (6)$$

Such an approach is, however, limited to small systems due to the exponential increase of the basis with system size. For example, for a system of $N = 75$ sites hosting $N_{\text{FM}} = 5$ localized spin-$\frac{1}{2}$, onto which a spin-polarized current pulse composed of $N_e = 8$ electrons is impinging in Fig. 2(b), the vectors and matrices in Eq. (6) have size $\binom{2N}{N_e}2^{N_{\text{FM}}} \approx 1.68 \times 10^{14}$.

To overcome this unfavorable scaling, we employ adaptive tDMRG framework [44–48] for which computational complexity is polynomial (instead of exponential) in system size. Let us first recall that the ground state DMRG [52–54] method can provide extremely accurate results for a many-body Hamiltonian [such as $\hat{H}$ in Eq. (1)]. The premise is to obtain a wave function that approximates the actual ground state in a reduced Hilbert space. The proposed solution has the very peculiar form of a "matrix-product state" (MPS) [55]

$$|\Psi\rangle = \sum_{\{s\}} A[s_1]_{\alpha_1} A[s_2]_{\alpha_1,\alpha_2}\dots A[s_{N-1}]_{\alpha_{N-1}\alpha_N}$$
$$\times A[s_N]_{\alpha_N}|s_1\dots s_N\rangle, \quad (7)$$

where the coefficients of an MPS are generated by contracting matrices A that are identified by a label corresponding to the state of the physical degree of freedom (the spin s, for instance). The row and column indices of the matrices correspond to the so-called "bond indices," with a "bond dimension" χ, also referred to as the number of DMRG basis states. One has to find the coefficients of this wave function variationally, and the DMRG is one way to do it efficiently. The accuracy of the wave function increases with the bond dimension and can be made asymptotically exact, as this bond dimension approaches the total number of degrees of freedom. Most importantly, no *a priori* assumptions are made about the form of the coefficients or the underlying physics. The power of the method is precisely that it is "smart" enough to be able to find for us the best possible candidate wave function of that form. Moreover, it can find numerically exact results (within machine precision) even with small matrices (small bond dimension). Even though the accuracy is finite, it is under control, so that we can obtain results that are essentially exact by just increasing the matrix size.

The generalization of DMRG to time-dependent problems requires one to iteratively optimize the matrices, which is known as the adaptive tDMRG algorithm, such that the balanced least-squares representation of the wave function is achieved for the whole time interval of propagation. We use the adaptive tDMRG formulation of Ref. [44], where the small-time evolution operator is decomposed into

$$e^{-i\hat{H}\delta t/\hbar} \approx e^{-i\hat{H}_1\delta t/2\hbar}\dots e^{-i\hat{H}_{N-1}\delta t/2\hbar}$$
$$\times e^{-i\hat{H}_{N-1}\delta t/2\hbar}\dots e^{-i\hat{H}_1\delta t/2\hbar}, \quad (8)$$

for an arbitrary many-body Hamiltonian $\hat{H} = \sum_{i=1}^{N-1} \hat{H}_i$ with nearest-neighbor interactions between N sites and $\hat{H}_i$ denoting its term on the bond i. Such approximation incurs an error of the order $O(\delta t^3)$. The small time step is chosen as $\delta t = 0.1\hbar/\gamma$. We start the propagation with $\chi = 100$ states and limit the truncation error to 10^{-7}, while the maximal number of states allowed during the evolution is set to $\chi_{\max} = 400$.

For $t \geq 0$, $\hat{H}_{V,\mathbf{B}} \equiv 0$ so that spin-polarized conduction electrons spread out from the region of N_{conf} sites and are injected into the FM chain. This process is illustrated schematically in Fig. 2(b), while the local charge and spin-z densities are computed numerically in Fig. 3 and animated in the tDMRG-computed movie in Supplemental Material [18]. Since fermionic leads are not semi-infinite as in the usual single-particle quantum transport calculations [16,19–24], the many-body system composed of

conduction electrons and localized spins can be evolved only for a limited time [49,50] before electrons are back-scattered by the right boundary which breaks $L \to R$ current flow. For example, in Fig. 3, such backscattering occurs at $t \simeq 40\hbar/\gamma$ for $N_e = 8$ injected electrons. Nevertheless, the quantum dynamics of flowing electron spins and localized spins captured by tDMRG calculations before the boundary reflection is fully equivalent to that in an open quantum system.

IV. PURELY QUANTUM SPIN-TRANSFER TORQUE IN COLLINEAR GEOMETRY

In the collinear setup [11,12], as one of the generators of purely quantum STT, the spin polarization of the injected conduction electrons is collinear but antiparallel to that of the localized spins at $t = 0$. In the Fock space sector with zero electrons $N_e = 0$, the many-body quantum state $|\Psi(t)\rangle$ for $t \geq 0$ within $\mathcal{F}_e \otimes \mathcal{H}_{\text{lspins}}$ space is trivially $|\Psi(t)\rangle = |\text{vac}\rangle_e \otimes |\Phi\rangle_{\text{lspins}}$, where the first factor of such a separable quantum state is the electron vacuum state $|\text{vac}\rangle_e \in \mathcal{F}_e$ and the second factor $|\Phi\rangle_{\text{lspins}} = |\downarrow_1\dots\downarrow_{N_{\text{FM}}}\rangle \in \mathcal{H}_{\text{lspins}}$ is the ground state of the FM chain. The Fock space sector $N_e = 1$ has been studied for an infinite ($N_{\text{FM}} \to \infty$) metallic FM chains long before [56] theoretical predictions for STT, but with the focus on magnetic polarons as the bound state of the injected electron and low-energy excitations (spinons or magnons) of all localized spins. In such a case, and for a FM chain [39,40] of finite length, we find $|\Psi(t\geq0)\rangle = c_0(t)|\text{orb}\rangle \otimes |\uparrow_e\rangle \otimes |\Phi\rangle + c_1(t)|\text{orb}\rangle \otimes |\downarrow_e\rangle \otimes |\uparrow_1\dots\downarrow_{N_{\text{FM}}}\rangle + \dots + c_{N_{\text{FM}}}(t) |\text{orb}\rangle \otimes |\downarrow_e\rangle \otimes |\downarrow_1\dots\uparrow_{N_{\text{FM}}}\rangle$. This superposition is constructed by including *all possible states* allowed by the conservation of the z component of total spin:

$$[\hat{H}, \hat{s}_e^z + \hat{S}_{\text{lspins}}^z] = 0, \quad (9)$$

where $\hat{S}_{\text{lspins}}^z = \hat{S}_1^z + \dots \hat{S}_{N_{\text{FM}}}^z$. Here, $|\text{orb}\rangle$ is orbital state of a single injected electron, and the coefficients $c_0(t), \dots, c_{N_{\text{FM}}}(t)$ studied in Ref. [39] can be much more complicated than those for magnons (or spinons) in an infinite FM chain [56] due to different boundary conditions.

The quantum state $|\Psi(t)\rangle$ also defines the pure state density matrix $|\Psi(t)\rangle\langle\Psi(t)|$. Since such a state for $N_e \geq 1$ is a sum of separable states and, therefore, entangled, the quantum state of subsystems must be described by the reduced density matrix [27–29]. This description is exemplified by

$$\hat{\rho}_1 = \text{Tr}_{\text{other}}|\Psi(t)\rangle\langle\Psi(t)| = \frac{1}{2}[\hat{I} + \mathbf{S}_1 \cdot \hat{\boldsymbol{\sigma}}], \quad (10)$$

which is the density matrix of the first localized spin within the FM region in Fig. 2. It is obtained by partial trace over
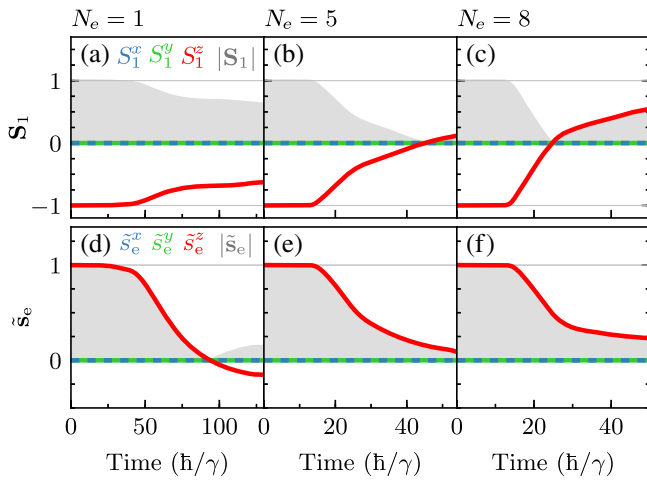
FIG. 4. Time evolution of the expectation value of first localized spin $\mathbf{S}_1 = (S_1^x, S_1^y, S_1^z)$ and the purity $|\mathbf{S}_1|$ of its quantum state (gray background) for a different number of injected electrons which are initially spin polarized along the $+z$ axis: (a) $N_e = 1$; (b) $N_e = 5$; and (c) $N_e = 8$. (d)–(f) plot average electron spin expectation value $\tilde{\mathbf{s}}_e = \mathbf{s}_e/N_e$ and purity $|\tilde{\mathbf{s}}_e|$. The sd exchange interaction between electron spin and localized spins is $J_{sd} = 0.5\gamma$. (c) and (f) are animated as the tDMRG-computed movie in Supplemental Material [18] for $J_{sd} = 0.5\gamma$ and $J_{sd} = 2.0\gamma$.

all states within $\mathcal{F}_e \otimes \mathcal{H}_{\text{lspins}}$ that are not in $\mathcal{H}_1$. Here, $\hat{I}$ is the unit 2×2 matrix, and $\hat{\boldsymbol{\sigma}} = (\hat{\sigma}^x, \hat{\sigma}^y, \hat{\sigma}^z)$ is the vector of the Pauli matrices. The magnitude $|\mathbf{S}_1|$ of the expectation value of localized spin-$\frac{1}{2}$,

$$\mathbf{S}_1 = \text{Tr}[\hat{\rho}_1 \hat{\boldsymbol{\sigma}}], \qquad (11)$$

also serves as *purity* specifying whether its quantum state is fully ($|\mathbf{S}_1| = 1$) or partially ($0 < |\mathbf{S}_1| < 1$) coherent. We use label $O \equiv \langle \hat{O} \rangle$ for the expectation value of an operator $\hat{O}$ in a pure many-body state of the total system electrons plus localized spins or in a mixed quantum state of a relevant (depending on observable $\hat{O}$) subsystem. Thus, *true* decoherence (i.e., decoherence that cannot be attributed to any classical noise [57]) due to many-body entanglement [27,28] can lead to reduction of local and total magnetization, $\mathbf{M}_i = g\mu_B \mathbf{S}_i$ and $\mathbf{M} = \sum_{i=1}^{N_{\text{FM}}} g\mu_B \mathbf{S}_i$, respectively, because of reduction of $\mathbf{S}_i$ expectation values. Such behavior is obviously forbidden [25,26] in classical magnetization dynamics described by the LLG equation [16,17,20].

The time evolution of $\mathbf{S}_1(t)$ is shown in Figs. 4(a)–4(c) for $N_e = 1, 5, 8$ injected electrons, respectively, as well as in the tDMRG-computed movie in Supplemental Material [18] for all $\mathbf{S}_i(t)$ using $N_e = 8$. Because of spin angular momentum conservation, only $S_i^z(t) \neq 0$. The magnetization reversal sought in spintronic applications [1,2], where $S_i^z(t)$ evolves from $S_i^z = -1$ at $t = 0$ to $S_i^z > 0$ at some later
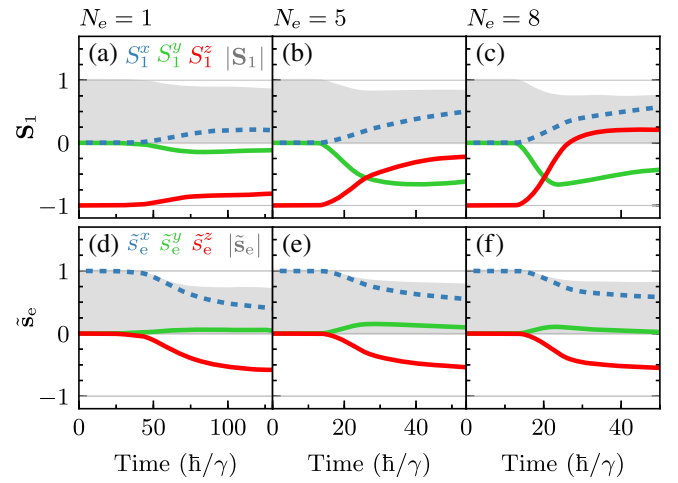
FIG. 5. (a)–(f) are counterparts of Figs. 4(a)–4(f), but for injected electrons which are spin polarized at $t < 0$ along the $+x$ axis. This polarization creates a noncollinear geometry of flowing and localized spins, as required for conventional STT [1].

time $t > 0$, occurs only when $N_e > N_{\text{FM}}$. The reversal is *nonclassical*, since $S_i^x(t) = S_i^y(t) \equiv 0$, unlike classical magnetization reversal [1,17,22], where $\mathbf{M}_i$ vectors must rotate away from the $-z$ axis to reach the $+z$ axis. The decoherence of localized spin states makes the reversal strikingly inhomogeneous (see the tDMRG-computed movie in Supplemental Material [18]), because localized spins away from the L-lead/FM-chain interface have smaller $|\mathbf{S}_i|$ or S_i^z can remain negative. The decoherence can be partially suppressed and all localized spins reversed by increasing J_{sd}, despite larger J_{sd} concurrently enhancing reflection of the current pulse at the L-lead/FM-chain interface (see the tDMRG-computed movie in Supplemental Material [18]). The spin expectation value per electron, $\tilde{\mathbf{s}}_e = \mathbf{s}_e/N_e$, plotted in Figs. 4(d)–4(f), shows that, due to many-body entanglement, electron spin states also decohere with purity $|\tilde{\mathbf{s}}_e| < 1$.

V. QUANTUM AND CONVENTIONAL SPIN-TRANSFER TORQUE IN NONCOLLINEAR GEOMETRY

As a comparison with purely quantum STT analyzed in Sec. IV for collinear setup, in Fig. 5, we apply tDMRG framework to noncollinear setup where conventional STT also exists [Fig. 1(b)] due to injected electrons being spin polarized along the $+x$ axis while localized spins are polarized along the $-z$ axis. Although this setup is considered [11,12] as a completely different situation from quantum STT in a collinear geometry, the state $|\rightarrow_e^x\rangle$ in quantum language corresponds to the injection of a superposition of spin-up and spin-down states, $|\rightarrow_e^x\rangle = (|\uparrow_e\rangle + |\downarrow_e\rangle)/\sqrt{2}$. In this case, we find in Figs. 5(a)–5(c) how localized spins always rotate, $S_i^x \neq 0$ and $S_i^y \neq 0$, away from the easy z axis for $t \geq 0$ akin to classical localized
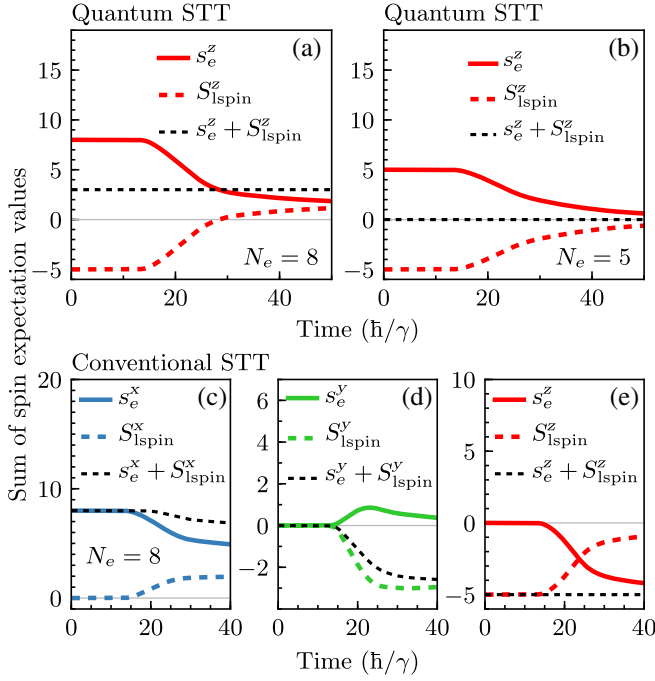
FIG. 6.   Time evolution of the sum of spin expectation values of all $N_{\mathrm{FM}} = 5$ localized spins $S^z_{\mathrm{lspins}}(t)$ and all injected (a) $N_e = 8$ or (b) $N_e = 5$ electrons $s^z_e(t)$ in collinear and antiparallel setup of quantum STT analyzed in Figs. 4(b), 4(c), 4(e), and 4(f). The same time evolution, but for noncollinear setup of conventional STT using $N_e = 8$ as analyzed in Figs. 5(c) and 5(f), is shown in (c)–(e). The z component of total spin is manifestly conserved (dashed blacked line) in (a), (b), and (e).

spins [1,17,22]. However, $|\mathbf{S}_1| < 1$ in Figs. 5(a)–5(c) signifies the same decoherence due to many-body entanglement found for quantum STT in Fig. 4.

VI. WHAT IS "TRANSFERRED" IN SPIN-TRANSFER TORQUE?

The conventional STT is commonly computed using some type of single-particle steady-state quantum transport formalism [19,20,22] to obtain the nonequilibrium electron spin density $\mathbf{s}_i$ injected into the FM-analyzer. Because of noncollinearity between $\mathbf{s}_i$ and the classical magnetization $\mathbf{M}$ of the FM-analyzer, contributions to $\mathbf{s}_i$ from propagating states oscillate as a function of position without decaying. Nevertheless, the transverse (with respect to $\mathbf{M}$) component of $\mathbf{s}_i$ is brought to zero within ∼1 nm away from the normal-metal/FM-analyzer interface by averaging over propagating states with different incoming momenta $\hbar\mathbf{k}$, because the frequency of spatial oscillations rapidly changes with $\mathbf{k}$ [19]. The angular dependence of STT ∝ $\sum_i \mathbf{s}_i \times \mathbf{M}$ can be fed [20,22] into the LLG calculations, which often consider only the macrospin [1,17,58] $\mathbf{M} = \sum_i \mathbf{M}_i$. Thus, in this picture, the microscopic mechanism of how spin angular momentum is transferred from electron subsystem to magnetization remains hidden.

The tDMRG simulations unveil such a mechanism in Figs. 6(a) and 6(b) for quantum STT, as well as in Figs. 6(c)–6(e) for conventional STT, where the total spin of all electrons $s^z_e(t)$ decays in time while the total spin of all localized spins $S^z_{\mathrm{lspins}}(t)$ increases as injected flowing spins try to align localized spins in the same direction. Figures 6(a), 6(b), and 6(e) also validate our calculations by confirming that $s^z_e(t) + S^z_{\mathrm{lspins}}(t)$ remains constant, as expected from the conservation law in Eq. (9). Because of the complex superposition of many-body states of electrons plus localized spins, the quantum dynamics of localized spins is always highly inhomogeneous and, therefore, quite different from the macrospin approximation [17] or simple spin-wave excitations [58] assumed in the modeling of classical magnetization dynamics driven by conventional STT.

VII. DYNAMICAL BUILDUP OF LONG-RANGE ENTANGLEMENT

The nonequilibrium many-body states of electrons and localized spins generated by STT exhibit (Fig. 7) growth of entanglement entropy [31,59]. Using entanglement measures [27,28] beyond entropy, we also predict that they will exhibit long-range [27,28] entanglement (Fig. 8). Massively and long-range entangled many-body quantum states have been sought among ground states of exotic phases of solid-state materials [27,28,34] and synthetic quantum matter like Rydberg atoms and trapped ions [60]. In the latter case, entanglement growth has been measured experimentally [31] in a system of ∼10 trapped ion qubits. To quantify entanglement growth as a function of time, we compute the time evolution of the standard [27,28,59] von Neumann entanglement entropy for half of the system:

$$\mathcal{S}_{(N+1)/2}(t) = -\mathrm{Tr}[\hat{\rho}_{(N+1)/2}(t) \ln \hat{\rho}_{(N+1)/2}(t)], \quad (12)$$

where $\hat{\rho}_{(N+1)/2}(t)$ is a many-body density matrix of a subsystem composed of three localized spins and of all electrons residing at time t within the first 38 sites of the system in Fig. 2. In addition, we also calculate the so-called Meyer-Wallach (MW) measure [28] of global entanglement [61], which is defined for a multipartite quantum system composed of two-level subsystems as

$$Q_{\mathrm{MW}} = 2\left(1 - \frac{1}{N_{\mathrm{FM}} + N_e}\left[\sum_{i=1}^{N_{\mathrm{FM}}} \mathrm{Tr}\hat{\rho}_i^2 + \sum_{j=1}^{N_e} \mathrm{Tr}\hat{\rho}_{e,j}^2\right]\right). \quad (13)$$

It quantifies average entanglement of each subsystem with the remaining $N_{\mathrm{FM}} + N_e - 1$ spins. The nonequilibrium dynamics driven by quantum STT and local interactions in the Hamiltonian in Eq. (1) conspire to increase both $\mathcal{S}_{(N+1)/2}$ [Fig. 7(a)] and $Q_{\mathrm{MW}}(t)$ [Fig. 7(b)]. The latter stays slightly below its maximum possible value $Q_{\mathrm{MW}} = 1$ (obtained for $\mathrm{Tr}\hat{\rho}_i^2 = \mathrm{Tr}\hat{\rho}_{e,j}^2 = 0$) when $N_e > N_{\mathrm{FM}}$ because
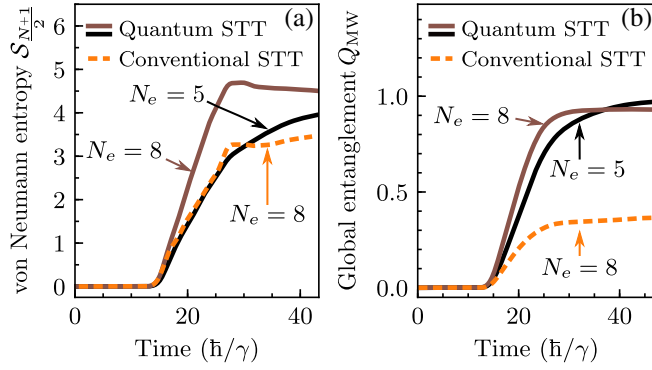
FIG. 7. (a) Time evolution of the von Neumann entropy [Eq. (12)] of half of the whole system in Fig. 2, which includes all electrons at time t within the first 38 sites and three of localized spins within the FM region. (b) Time evolution of global entanglement measure [Eq. (13)] for a subsystem composed of all conduction electron spins and all localized spins.

of the initial condition $s_e^z + S_{\text{lspins}}^z \neq 0$. Both $\mathcal{S}_{(N+1)/2}(t)$ and $Q_{\text{MW}}(t)$ reach smaller asymptotic values (Fig. 7) at longer times in the case of conventional STT in noncollinear geometry, so that they clearly differentiate between purely quantum and conventional STT.

For the purpose of demonstrating dynamical buildup of long-range entanglement in nonequilibrium quantum many-body states generated by quantum STT, we additionally analyze the mutual information [28]

$$\mathcal{I}(1|N_{\text{FM}}) = \mathcal{S}_1 + \mathcal{S}_{N_{\text{FM}}} - \mathcal{S}_{1,N_{\text{FM}}} \quad (14)$$

between localized spins at the edge of the FM region, i.e., at sites 1 and N_{FM}. Here, $\mathcal{S}_1$ is the von Neumann entropy computed via Eq. (12) from the density matrix $\hat{\rho}_1$ [Eq. (10)] of localized spin 1 at the left edge of FM; $\mathcal{S}_{N_{\text{FM}}}$ is the von Neumann entropy of localized spin at the right edge of the FM region; and $\mathcal{S}_{1,N_{\text{FM}}}$ is the von Neumann entropy of a subsystem composed of these two localized spins. The three entropies are evaluated for a many-body state generated after N_e electrons are injected into FM with $N_{\text{FM}} = N_e$ localized spins, so that at $t = 0$ the state is separable: $|\Psi(t = 0)\rangle = |\text{orb}\rangle \otimes |\uparrow_e \uparrow_e ... \uparrow_e\rangle \otimes |\downarrow_1 \downarrow_2 ... \downarrow_{N_{\text{FM}}}\rangle$. To show explicitly the type of state generated and also to be able to analyze its properties in the limit $N_{\text{FM}} \to \infty$, we do not evolve the initial state by tDMRG but instead write for $t > 0$

$$|\Psi(t \geq 0)\rangle = |\text{orb}\rangle \otimes \frac{1}{\sqrt{C}} (|\uparrow_e \uparrow_e ... \uparrow_e\rangle \otimes |\downarrow_1 \downarrow_2 ... \downarrow_{N_{\text{FM}}}\rangle$$
$$+ |\downarrow_e \uparrow_e ... \uparrow_e\rangle \otimes |\uparrow_1 \downarrow_2 ... \downarrow_{N_{\text{FM}}}\rangle + \cdots$$
$$+ |\downarrow_e \downarrow_e ... \uparrow_e\rangle \otimes |\uparrow_1 \uparrow_2 ... \downarrow_{N_{\text{FM}}}\rangle + \cdots$$
$$+ |\downarrow_e \downarrow_e ... \downarrow_e\rangle \otimes |\uparrow_1 \uparrow_2 ... \uparrow_{N_{\text{FM}}}\rangle). \quad (15)$$
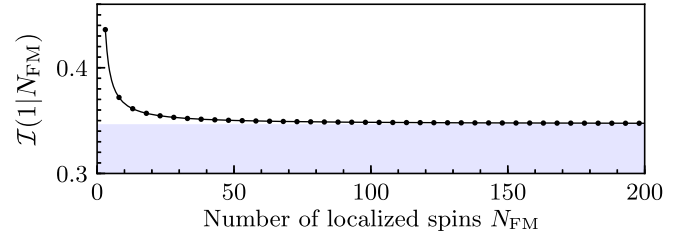

FIG. 8. Mutual information $\mathcal{I}(1|N_{\text{FM}})$ [Eq. (14)] between localized spins 1 and N_{FM} at the edges of FM region in Fig. 2 as a function of its length N_{FM}. The entangled nonequilibrium many-body state characterized by $\mathcal{I}(1|N_{\text{FM}})$ is generated by quantum STT exerted by $N_e = N_{\text{FM}}$ injected electrons [with the simplification that all possible terms in this state enter with equal weight in Eq. (15)]. In the limit of infinite separation between the edges, as $N_{\text{FM}} \to \infty \Rightarrow \mathcal{I}(1|N_{\text{FM}}) \to (\ln 2)/2$.

The individual terms in this sum are *all possible* separable states *obeying* the spin conservation law in Eq. (9), where we employ simplification that coefficients in front of each term are identical and time independent. Our tDMRG simulation effectively generates proper nonuniform [39] time-dependent coefficients, and it can be conducted for $N_{\text{FM}} = N_e \sim 100$, but the state in Eq. (15) can be written and analyzed for arbitrarily large N_{FM}. There are $C = \binom{2N_{\text{FM}}}{N_{\text{FM}}} \sim 4^{N_{\text{FM}}}/\sqrt{N_{\text{FM}}}$ terms in the sum in Eq. (15). Thus, the subspace of dimension $\sim 4^{N_{\text{FM}}}/\sqrt{N_{\text{FM}}}$ capturing time evolution of nonequilibrium states of the type in Eq. (15) also furnishes an example where the majority of all possible $4^{N_{\text{FM}}}$ states in the Hilbert space are unphysical in the sense of not being utilized in the course of time evolution [62].

The von Neumann entropies of the edge localized spins, $\mathcal{S}_1 = \mathcal{S}_{N_{\text{FM}}+1} = \ln 2$, are obtained from $\hat{\rho}_1 = \frac{1}{2}(|\uparrow_1\rangle\langle\uparrow_1| + |\downarrow_1\rangle\langle\downarrow_1|)$ as an incoherent mixture with zero off-diagonal elements, while

$$\mathcal{S}_{1,N_{\text{FM}}} = \frac{N_{\text{FM}}}{2N_{\text{FM}} - 1} \ln \frac{2N_{\text{FM}} - 1}{N_{\text{FM}}}$$
$$+ \frac{N_{\text{FM}} - 1}{2N_{\text{FM}} - 1} \ln \frac{4N_{\text{FM}} - 2}{N_{\text{FM}} - 1} \quad (16)$$

is obtained from Eq. (12) using $\hat{\rho}_{1,N_{\text{FM}}} = \text{Tr}_{\text{other}}|\Psi\rangle\langle\Psi|$ that contains also nonzero off-diagonal elements. The coherences encoded by the off-diagonal elements lead to nonzero mutual information in Fig. 8 even at *infinite* separation between the edge spins:

$$\lim_{N_{\text{FM}} \to \infty} \mathcal{I}(1|N_{\text{FM}}) = \frac{\ln 2}{2}, \quad (17)$$

as the signature of *long-range entanglement*. This result demonstrates that pure nonequilibrium many-body states of the type displayed in Eq. (15) is *macroscopically* entangled and quantum correlated. Notice that this entanglement

persists even as the electrons leave FM region and are no longer interacting with the localized spins, as demonstrated by the tDMRG-computed movie in Supplemental Material [18].

VIII. CONCLUSIONS AND OUTLOOK

In conclusion, we introduce tDMRG as a fully quantum many-body framework for describing transfer of spin angular momentum between flowing electrons, comprising a current pulse, and localized spins. Unlike the standard model approaches to conventional Slonczewski-Berger STT [1,16,20,23,24], which are all based on single-particle quantum mechanics for electrons and classical LLG description of localized spins, tDMRG can describe spin transfer even when such approaches predict *completely absent* STT. This description includes experimentally explored collinear but antiparallel localized and flowing spins in spin valves [11] or in schemes exciting high-energy magnons [13–15], as well as possible future experiments on spin-polarized current injection into strongly electron-correlated materials like quantum antiferromagnets [32,33] and Mott insulators [32] or exotic materials like quantum spin liquids [34] where the expectation value of localized spins is zero in equilibrium. In all of these situations, a classical LLG equation description of localized spins is inapplicable due to many-body entanglement [27,28] in either an equilibrium state or in a nonequilibrium quantum many-body state (or both) of all flowing electrons and localized spins. The entanglement entropy of nonequilibrium quantum many-body state driven by quantum STT grows in time (Fig. 7), while the state additionally becomes long-range entangled (Fig. 8). Thus, instead of LLG dynamics of classical vectors assumed to mimic trajectories of the quantum-mechanical spin expectation values, such a nonequilibrium quantum many-body state must be evolved and expectation values of localized spins computed only at the end—*we term any such situation quantum STT.*

Looking to the future, since tDMRG is limited to 1D and quasi-1D (such as two-leg ladders [47]) systems, modeling of quantum STT in two-dimensional [22] and three-dimensional [20] realistic spintronic devices over long times requires one to develop many-body NEGF-based algorithms [63] (as opposed to presently widely used single-particle NEGF algorithms [16,20–24] applied to conventional STT) where a number of technical challenges [41,43] remain to be solved. For such necessarily perturbative efforts, our tDMRG approach to quantum STT offers rigorous nonperturbative benchmarking [63] using 1D examples like the one in Fig. 2.

Although experimental measurement of many-body entanglement [27,28] has been achieved in cold gases of ~10 atoms using atomic-molecular-optical physics techniques [31], it remains an outstanding challenge [27] for solid-state materials and devices. For the special case of quantum-STT-driven many-body entanglement in nonequilibrium spintronic devices studied here, we propose that, by injecting an electronic current pulse of sufficient magnitude, many-body entanglement of a macroscopically large number of flowing and localized spins can be detected: (i) by first measuring the spectrum of excitations via inelastic light scattering (Raman or Brillouin) [64] of the FM-analyzer layer in equilibrium, where magnons peaks will be observed; (ii) immediately after the pulse has ceased, measure the spectrum of excitations again where a broad continuum [34] could be observed due to long-range entangled (Fig. 8) localized spins of the FM-analyzer. Beyond spintronics, STT-driven quantum dynamics of localized spins can be employed [65] to manipulate individual spin qubits and entangle them over very long distances.

ACKNOWLEDGMENTS

[1] D. Ralph and M. Stiles, *Spin Transfer Torques*, J. Magn. Magn. Mater. **320**, 1190 (2008).

[2] N. Locatelli, V. Cros, and J. Grollier, *Spin-Torque Building Blocks*, Nat. Mater. **13**, 11 (2014).

[3] J. C. Slonczewski, *Current-Driven Excitation of Magnetic Multilayers*, J. Magn. Magn. Mater. **159**, L1 (1996).

[4] L. Berger, *Emission of Spin Waves by a Magnetic Multilayer Traversed by a Current*, Phys. Rev. B **54**, 9353 (1996).

[5] M. Tsoi, A. G. M. Jansen, J. Bass, W.-C. Chiang, M. Seck, V. Tsoi, and P. Wyder, *Excitation of a Magnetic Multilayer by an Electric Current*, Phys. Rev. Lett. **80**, 4281 (1998).

[6] E. B. Myers, D. C. Ralph, J. A. Katine, R. N. Louie, and R. A. Buhrman, *Current-Induced Switching of Domains in Magnetic Multilayer Devices*, Science **285**, 867 (1999).

[7] J. A. Katine, F. J. Albert, R. A. Buhrman, E. B. Myers, and D. C. Ralph, *Current-Driven Magnetization Reversal and Spin-Wave Excitations in* Co/Cu/Co *Pillars*, Phys. Rev. Lett. **84**, 3149 (2000).

[8] J. C. Sankey, Y.-T. Cui, J. Z. Sun, J. C. Slonczewski, R. A. Buhrman, and D. C. Ralph, *Measurement of the Spin-Transfer-Torque Vector in Magnetic Tunnel Junctions*, Nat. Phys. **4**, 67 (2008).

[9] H. Kubota, A. Fukushima, K. Yakushiji, T. Nagahama, S. Yuasa, K. Ando, H. Maehara, Y. Nagamine, K. Tsunekawa, D. D. Djayaprawira, N. Watanabe, and Y. Suzuki, *Quantitative Measurement of Voltage Dependence of*

Spin-Transfer Torque in MgO-Based Magnetic Tunnel Junctions, Nat. Phys. **4**, 37 (2008).

[10] C. Wang, Y.-T. Cui, J. A. Katine, R. A. Buhrman, and D. C. Ralph, *Time-Resolved Measurement of Spin-Transfer-Driven Ferromagnetic Resonance and Spin Torque in Magnetic Tunnel Junctions,* Nat. Phys. **7**, 496 (2011).

[11] A. Zholud, R. Freeman, R. Cao, A. Srivastava, and S. Urazhdin, *Spin Transfer due to Quantum Magnetization Fluctuations,* Phys. Rev. Lett. **119**, 257201 (2017).

[12] S. Zhang, *Viewpoint: Quantum Spin Torque,* Physics **10**, 135 (2017).

[13] T. Balashov, A. F. Takács, M. Däne, A. Ernst, P. Bruno, and W. Wulfhekel, *Inelastic Electron-Magnon Interaction and Spin Transfer Torque,* Phys. Rev. B **78**, 174404 (2008).

[14] K. J. Kim, T. Moriyama, T. Koyama, D. Chiba, S. W. Lee, S. J. Lee, K. J. Lee, H. W. Lee, and T. Ono, *Current-Induced Asymmetric Magnetoresistance due to Energy Transfer via Quantum Spin-Flip Process,* arXiv:1603.08746.

[15] K.-J. Kim, T. Li, S. Kim, T. Moriyama, T. Koyama, D. Chiba, K.-J. Lee, H.-W. Lee, and T. Ono, *Possible Contribution of High-Energy Magnons to Unidirectional Magnetoresistance in Metallic Bilayers,* Appl. Phys. Express **12**, 063001 (2019).

[16] M. D. Petrović, B. S. Popescu, U. Bajpai, P. Plecháč, and B. K. Nikolić, *Spin and Charge Pumping by a Steady or Pulse-Current-Driven Magnetic Domain Wall: A Self-Consistent Multiscale Time-Dependent Quantum-Classical Hybrid Approach,* Phys. Rev. Applied **10**, 054038 (2018).

[17] D. V. Berkov and J. Miltat, *Spin-Torque Driven Magnetization Dynamics: Micromagnetic Modeling,* J. Magn. Magn. Mater. **320**, 1238 (2008).

[18] See Supplemental Material at http://link.aps.org/supplemental/10.1103/PhysRevX.11.021062 for a tDMRG-computed movie which animates (for two different values of J_{sd}) Figs. 3 and 4. It depicts time dependences $\mathbf{S}_1(t), ... \mathbf{S}_5(t)$ for all five localized spins, as well as time evolution $\mathbf{s}_i(t)$ of spin density at site i generated by spin-polarized electrons injected into the FM region in Fig. 2. The FM region of localized spins in the movies is denoted by a gray rectangle. Electrons are initially ($t < 0$) spin polarized along the $+z$ axis, while localized spins are polarized along the $-z$ axis. The bottom panels in the movie show time evolution of charge density as it spreads from the region of N_{conf} sites in Fig. 2(a) into the FM region, thereby animating Fig. 3(a). In addition, we provide three pedagogical movies which animate Figs. 1(a), 1(b), and 1(c), respectively, using quantum-classical TDNEGF + LLG formalism [20–22] to demonstrate rigorously that no conventional-STT-driven dynamics of localized spins, viewed as classical vectors $\mathbf{S}_i(t)$ of fixed length, is possible in the collinear setups of Figs. 1(a) and 1(c). In these three movies, the top three panels show time evolution of voltage pulse [22], nonequilibrium electronic spin density $\mathbf{s}_1(t)$ on the first site of the FM-analyzer, and conventional STT $\mathbf{T}_1(t) \propto \mathbf{s}_1(t) \times \mathbf{S}_1(t)$ on localized spin $\mathbf{S}_1(t)$ on that first site, respectively, while the bottom panel shows time evolution of the components of all three localized spins $\mathbf{S}_i(t)$ within the FM-analyzer layer of FM-polarizer/normal-metal/FM-analyzer spin valve.

[19] S. Wang, Y. Xu, and K. Xia, *First-Principles Study of Spin-Transfer Torques in Layered Systems with Noncollinear Magnetization,* Phys. Rev. B **77**, 184430 (2008).

[20] M. O. A. Ellis, M. Stamenova, and S. Sanvito, *Multiscale Modeling of Current-Induced Switching in Magnetic Tunnel Junctions Using Ab Initio Spin-Transfer Torques,* Phys. Rev. B **96**, 224410 (2017).

[21] K. D. Belashchenko, A. A. Kovalev, and M. van Schilfgaarde, *First-Principles Calculation of Spin-Orbit Torque in a Co/Pt Bilayer,* Phys. Rev. Mater. **3**, 011401(R) (2019).

[22] K. Dolui, M. D. Petrović, K. Zollner, P. P. Plecháč, J. Fabian, and B. K. Nikolić, *Proximity Spin-Orbit Torque on a Two-Dimensional Magnet within van der Waals Heterostructure: Current-Driven Antiferromagnet-to-Ferromagnet Reversible Nonequilibrium Phase Transition in Bilayer* CrI_3, Nano Lett. **20**, 2288 (2020).

[23] U. Bajpai and B. K. Nikolić, *Time-Retarded Damping and Magnetic Inertia in the Landau-Lifshitz-Gilbert Equation Self-Consistently Coupled to Electronic Time-Dependent Nonequilibrium Green Functions,* Phys. Rev. B **99**, 134409 (2019).

[24] A. Suresh, U. Bajpai, M. D. Petrović, H. Yang, and B. K. Nikolić, *Magnon- versus Electron-Mediated Spin-Transfer Torque Exerted by Spin Current across an Antiferromagnetic Insulator to Switch the Magnetization of an Adjacent Ferromagnetic Metal,* Phys. Rev. Applied **15**, 034089 (2021).

[25] R. Wieser, *Description of a Dissipative Quantum Spin Dynamics with a Landau-Lifshitz-Gilbert like Damping and Complete Derivation of the Classical Landau-Lifshitz Equation,* Eur. Phys. J. B **88**, 77 (2015).

[26] R. Wieser, *Derivation of a Time Dependent Schrödinger Equation as the Quantum Mechanical Landau-Lifshitz-Bloch Equation,* J. Phys. Condens. Matter **28**, 396003 (2016).

[27] N. Laflorencie, *Quantum Entanglement in Condensed Matter Systems,* Phys. Rep. **646**, 1 (2016).

[28] G. De Chiara and A. Sanpera, *Genuine Quantum Correlations in Quantum Many-Body Systems: A Review of Recent Progress,* Rep. Prog. Phys. **81**, 074002 (2018).

[29] A. Elben, R. Kueng, H.-Y. (Robert) Huang, R. van Bijne, C. Kokail, M. Dalmonte, P. Calabrese, B. Kraus, J. Preskill, P. Zoller, and B. Vermersch, *Mixed-State Entanglement from Local Randomized Measurements,* Phys. Rev. Lett. **125**, 200501 (2020).

[30] B. Skinner, J. Ruhman, and A. Nahum, *Measurement-Induced Phase Transitions in the Dynamics of Entanglement,* Phys. Rev. X **9**, 031009 (2019).

[31] T. Brydges, A. Elben, P. Jurcevic, B. Vermersch, C. Maier, B. P. Lanyon, P. Zoller, R. Blatt, and C. F. Roos, *Probing Rényi Entanglement Entropy via Randomized Measurements,* Science **364**, 260 (2019).

[32] M. D. Petrović, P. Mondal, A. E. Feiguin, and B. K. Nikolić, *Quantum Spin Torque Driven Transmutation of Antiferromagnetic Mott Insulator,* Phys. Rev. Lett. **126**, 197202 (2021).

[33] A. Mitrofanov and S. Urazhdin, *Nonclassical Spin Transfer Effects in an Antiferromagnet,* Phys. Rev. Lett. **126**, 037203 (2021).

[34] C. Broholm, R. J. Cava, S. A. Kivelson, D. G. Nocera, M. R. Norman, and T. Senthil, *Quantum Spin Liquids,* Science **367**, eaay0668 (2020).

[35] Y. Wang and L. J. Sham, *Quantum Approach of Mesoscopic Magnet Dynamics with Spin Transfer Torque*, Phys. Rev. B **87**, 174433 (2013).

[36] T. Tay and L. J. Sham, *Theory of Atomistic Simulation of Spin-Transfer Torque in Nanomagnets*, Phys. Rev. B **87**, 174407 (2013).

[37] A. Qaiumzadeh and A. Brataas, *Quantum Magnetization Fluctuations via Spin Shot Noise*, Phys. Rev. B **98**, 220408(R) (2018).

[38] S. A. Bender, R. A. Duine, and Y. Tserkovnyak, *Quantum Spin-Transfer Torque and Magnon-Assisted Transport in Nanostructures*, Phys. Rev. B **99**, 024434 (2019).

[39] P. Mondal, U. Bajpai, M. D. Petrović, P. Plecháč, and B. K. Nikolić, *Quantum Spin Transfer Torque Induced Nonclassical Magnetization Dynamics and Electron-Magnetization Entanglement*, Phys. Rev. B **99**, 094431 (2019).

[40] A. Mitrofanov and S. Urazhdin, *Energy and Momentum Conservation in Spin Transfer*, Phys. Rev. B **102**, 184402 (2020).

[41] F. Mahfouzi and B. K. Nikolić, *Signatures of Electron-Magnon Interaction in Charge and Spin Currents through Magnetic Tunnel Junctions: A Nonequilibrium Many-Body Perturbation Theory Approach*, Phys. Rev. B **90**, 045115 (2014).

[42] M. Vogl, P. Laurell, H. Zhang, S. Okamoto, and G. A. Fiete, *Resummation of the Holstein-Primakoff Expansion and Differential Equation Approach to Operator Square Roots*, Phys. Rev. Research **2**, 043243 (2020).

[43] U. Bajpai, A. Suresh, and B. K. Nikolić, *Quantum Many-Body States and Green Functions of Nonequilibrium Electron-Magnon Systems: Localized Spin Operators vs. Their Mapping to Holstein-Primakoff Bosons*, arXiv:2104.07657.

[44] S. R. White and A. E. Feiguin, *Real-Time Evolution Using the Density Matrix Renormalization Group*, Phys. Rev. Lett. **93**, 076401 (2004).

[45] P. Schmitteckert, *Nonequilibrium Electron Transport Using the Density Matrix Renormalization Group Method*, Phys. Rev. B **70**, 121302(R) (2004).

[46] A. J. Daley, C. Kollath, U. Schollwöck, and G. Vidal, *Time-Dependent Density-Matrix Renormalization-Group Using Adaptive Effective Hilbert Spaces*, J. Stat. Mech. (2004) P04005.

[47] A. E. Feiguin, *The Density Matrix Renormalization Group and Its Time-Dependent Variants*, AIP Conf. Proc. **1419**, 5 (2011).

[48] S. Paeckel, T. Köhler, A. Swoboda, S. R. Manmana, U. Schollwöck, and C. Hubig, *Time-Evolution Methods for Matrix-Product States*, Ann. Phys. (Amsterdam) **411**, 167998 (2019).

[49] F. Lange, S. Ejima, T. Shirakawa, S. Yunoki, and H. Fehske, *Spin Transport through a Spin-$\frac{1}{2}$ XXZ Chain Contacted to Fermionic Leads*, Phys. Rev. B **97**, 245124 (2018).

[50] F. Lange, S. Ejima, and H. Fehske, *Driving XXZ Spin Chains: Magnetic-Field and Boundary Effects*, Europhys. Lett. **125**, 17001 (2019).

[51] A. M. Tsvelik and O. M. Yevtushenko, *Chiral Spin Order in Kondo-Heisenberg Systems*, Phys. Rev. Lett. **119**, 247203 (2017).

[52] S. R. White, *Density Matrix Formulation for Quantum Renormalization Groups*, Phys. Rev. Lett. **69**, 2863 (1992).

[53] S. R. White, *Density-Matrix Algorithms for Quantum Renormalization Groups*, Phys. Rev. B **48**, 10345 (1993).

[54] U. Schollwöck, *The Density-Matrix Renormalization Group*, Rev. Mod. Phys. **77**, 259 (2005).

[55] S. Östlund and S. Rommer, *Thermodynamic Limit of Density Matrix Renormalization*, Phys. Rev. Lett. **75**, 3537 (1995).

[56] B. S. Shastry and D. C. Mattis, *Theory of the Magnetic Polaron*, Phys. Rev. B **24**, 5340 (1981).

[57] J. Kayser, K. Luoma, and W. T. Strunz, *Geometric Characterization of True Quantum Decoherence*, Phys. Rev. A **92**, 052117 (2015).

[58] A. Brataas, Y. Tserkovnyak, and G. E. W. Bauer, *Current-Induced Macrospin versus Spin-Wave Excitations in Spin Valves*, Phys. Rev. B **73**, 014408 (2006).

[59] J. H. Bardarson, F. Pollmann, and J. E. Moore, *Unbounded Growth of Entanglement in Models of Many-Body Localization*, Phys. Rev. Lett. **109**, 017202 (2012).

[60] A. Elben, J. Yu, G. Zhu, M. Hafezi, F. Pollmann, P. Zoller, and B. Vermersch, *Many-Body Topological Invariants from Randomized Measurements in Synthetic Quantum Matter*, Sci. Adv. **6**, eaaz3666 (2020).

[61] A. Chandran, D. Kaszlikowski, A. Sen(De), U. Sen, and V. Vedral, *Regional versus Global Entanglement in Resonating-Valence-Bond States*, Phys. Rev. Lett. **99**, 170502 (2007).

[62] D. Poulin, A. Qarry, R. Somma, and F. Verstraete, *Quantum Simulation of Time-Dependent Hamiltonians and the Convenient Illusion of Hilbert Space*, Phys. Rev. Lett. **106**, 170501 (2011).

[63] N. Schlünzen, S. Hermanns, M. Scharnke, and M. Bonitz, *Ultrafast Dynamics of Strongly Correlated Fermions-Nonequilibrium Green Functions and Selfenergy Approximations*, J. Phys. Condens. Matter **32**, 103001 (2020).

[64] M. Arana, F. Estrada, D. S. Maior, J. B. S. Mendes, L. E. Fernandez-Outon, W. A. A. Macedo, V. M. T. S. Barthem, D. Givord, A. Azevedo, and S. M. Rezende, *Observation of Magnons in* Mn_2Au *Films by Inelastic Brillouin and Raman Light Scattering*, Appl. Phys. Lett. **111**, 192409 (2017).

[65] A. Bou Comas, E. M. Chudnovsky, and J. Tejada, *Manipulating Quantum Spins by Spin-Polarized Current: An Approach Based upon $\mathcal{PT}$-Symmetric Quantum Mechanics*, J. Phys. Condens. Matter **31**, 195801 (2019).